EES Catalysis

PAPER

View Article Online
View Journal | View Issue

Cite this: *EES Catal.*, 2025, 3, 1369

Stabilizing amorphous NiFe-based catalysts *via* borate bridging for water oxidation under industrial conditions†

Wei Qi,[ab] Youze Zeng,[ab] Liuqing Wang,[ab] Jinsheng Li,[b] Zhuoqi Wang,[ab] Feiyan An,[ab] Kai Li,[c] Meiling Xiao, *[abd] Changpeng Liu, [abd] Wei Xing *[abd] and Jianbing Zhu *[abd]

Received 28th May 2025,
Accepted 20th July 2025

DOI: 10.1039/d5ey00157a

rsc.li/eescatalysis

The practical deployment of an anion exchange membrane water electrolyzer (AEMWE) relies on the exploration of active and durable electrocatalysts towards the sluggish oxygen evolution reaction (OER). Although amorphous NiFe-based catalysts (a-$NiFeO_xH_y$) emerge as the competitive candidate due to impressive intrinsic OER activity, their unique defective structure renders the metal sites more susceptible to over-oxidation and dissolution, leading to poor stability. To address this challenge, we incorporate borate groups (BO_3^{3-}) into the a-$NiFeO_xH_y$ lattice by occupying the oxygen vacancy sites. The bridged borates not only maintain the structural stability *via* filling the oxygen vacancies, but also assist electron transfer from Ni to Fe to suppress Fe ion dissolution, thereby enhancing the catalytic stability of a-$NiFeO_xH_y$. Moreover, the tailored electronic structure of Ni favors electrochemical reconstruction to high-valence Ni active species and optimizes adsorption of oxygen intermediates towards superior OER activity. Therefore, a-B-$NiFeO_xH_y$ integrated into the AEMWE can deliver a noteworthy current density of 4.75 A cm^{-2} at a voltage of 2.0 V and maintain stable operation at 0.5 A cm^{-2} for 3000 hours. This study not only affords a promising electrocatalyst for the AEMWE, but also paves a new avenue to break the activity-stability trade-off of amorphous materials for the OER.

Broader context

With the global push toward carbon neutrality, hydrogen production *via* water electrolysis driven by renewable electricity is gaining increasing attention as a clean and sustainable energy solution. Anion exchange membrane water electrolysis (AEMWE) holds particular promise due to its potential to combine the low-cost catalysts of alkaline systems with the compact architecture of PEM electrolyzers. However, the slow kinetics and poor durability of the oxygen evolution reaction (OER) on the anode severely restrict the performance and long-term viability of AEMWE systems. Among the various catalysts explored, amorphous NiFe-based materials exhibit high OER activity but suffer from poor operational stability, especially under industrially relevant conditions such as high current density and elevated temperature. Breaking the long-standing trade-off between activity and stability remains a key challenge. This study addresses the stability issue of amorphous NiFe-based electrocatalysts for the OER by filling oxygen vacancies with borate anions (BO_3^{3-}). The tailored electronic states and strengthened Ni–O–Fe structure enable industrial current density and long-term stability over 3000 h in a practical water electrolyzer.

Introduction

The increasing global energy demand and the limited availability of fossil resources have driven a surge of interest in the development of sustainable energy conversion and storage technologies.[1] Water electrolysis powered by renewable electricity stands out as an ideal solution for the utilization and storage of intermittent renewable energy sources, such as solar and wind power, into green hydrogen, which aligns with global carbon neutrality targets.[2] Among the various water electrolysis technologies, anion exchange membrane water electrolysis (AEMWE) attracts particular attention as it can combine the

[a] *School of Applied Chemistry and Engineering, University of Science and Technology of China, Hefei, 230026, China*
[b] *State Key Laboratory of Electroanalytic Chemistry, Jilin Province Key Laboratory of Low Carbon Chemistry Power, Changchun Institute of Applied Chemistry, Chinese Academy of Sciences, Changchun, 130022, China. E-mail: mlxiao@ciac.ac.cn, xingwei@ciac.ac.cn, zjb@ciac.ac.cn*
[c] *State Key Laboratory of Rare Earth Resource Utilization, Changchun Institute of Applied Chemistry, Chinese Academy of Sciences, Changchun, 130022, China*
[d] *Chinese Academy of Sciences-HK Joint Laboratory for Hydrogen Energy, Changchun, 130022, China*

† Electronic supplementary information (ESI) available. See DOI: https://doi.org/10.1039/d5ey00157a

advantages of alkaline water electrolysis (AWE) and proton exchange membrane water electrolysis (PEMWE), *i.e.*, utilize non-precious metal electrocatalysts and zero-gap configuration.[3] However, the sluggish oxygen evolution reaction (OER) kinetics at the anode lead to a considerable voltage loss of AEMWE, thus significantly decreasing its energy conversion efficiency.[4] In this regard, developing highly efficient electrocatalysts to accelerate the OER kinetics is crucial to advancing AEMWE as a viable technology for sustainable hydrogen production.

The past decades have witnessed a blooming development of non-precious metal OER electrocatalysts, among which nickel–iron layered double hydroxides (NiFe-LDH) emerge as the most promising candidate due to their natural abundance, cost-effectiveness, and high catalytic activity.[5] To further improve their activity, a variety of strategies have been employed, including cation/anion doping, morphology engineering, hetero-interface construction, defect engineering and amorphization.[6] Notably, amorphization has been proven effective in boosting the OER activity of NiFe-LDH because the disordered structure of amorphous materials not only increases active site density by exposing abundant unsaturated edge sites, but also contributes to increased flexibility in the electronic structure towards optimized binding energy of oxygen-containing intermediates for the OER.[7] This structural flexibility also enables more efficient electron and proton transfer during the reaction, thus expediting the OER kinetics. Despite their improved catalytic activity, amorphous NiFe catalysts suffer from instability issues, primarily due to the oxidation and dissolution of metal ions, particularly Fe, at high anodic potential.[8] In fact, insufficient stability is the main bottleneck for the practical application of NiFe-LDH, and the amorphous structure aggravates this issue. What's worse, rapid degradation can occur at a larger current density (>500 mA cm^{-2}) and high temperature, which represents real operating conditions of AEMWE.[9] Therefore, how to break the activity-stability trade-off of the amorphous NiFe remains a critical challenge and requires urgent advancement to make these materials viable for practical applications in AEMWE.

Motivated by this challenge, we herein propose a borate anion (BO_3^{3-}) doping strategy for enhancing the stability of amorphous NiFe electrocatalysts. Owing to the intrinsic electron-deficient nature of boron atoms, they can act as effective electron transit centers to significantly promote the oxidation of Ni^{2+} to high-valent Ni species, thereby enhancing the OER activity. Meanwhile, the incorporation of BO_3^{3-} anions helps stabilize the metal–oxygen framework and fill oxygen vacancies, which effectively suppresses the dissolution of metal ions and improves the structural stability of the catalyst. Therefore, borate doping offers comprehensive advantages over conventional doping strategies in amorphous NiFe-based electrocatalysts. As a result, the optimized a-B-NiFeO$_x$H$_y$ catalyst exhibits remarkable OER stability, with negligible potential decay after 170 hours of continuous testing at 10 mA cm^{-2}, whereas the a-NiFeO$_x$H$_y$ catalyst shows a significant increase in voltage over the same period. More impressively, when integrated into a home-made AEMWE, a-B-NiFeO$_x$H$_y$ can deliver a high current density of 4.75 A cm^{-2} at 2.0 V and maintains long-term stability at 0.5 A cm^{-2} for 3000 h, demonstrating the huge application potential in the practical device. Combining *in situ* characterization with theoretical calculations, we unveil that the presence of BO_3^{3-} not only facilitates electron transfer from Ni to Fe to suppress the oxidation and dissolution of Fe during the OER but also tailors the adsorption strength of OER intermediates to propel the reaction kinetics, thereby endowing the a-B-NiFeO$_x$H$_y$ catalyst with significantly improved stability and activity.

Results and discussion

The amorphous borate-doped nickel–iron hydroxides (denoted as a-B-NiFeO$_x$H$_y$) were synthesized by a co-precipitation rapid-quenching method (Fig. 1a). In particular, a high-concentration solution of metal precursors with an optimal Ni/Fe ratio of 3 : 1 was quickly mixed with a 2 mol L^{-1} $NaBH_4$ alkaline solution under stirring, followed by immediately quenching the mixture solution in liquid nitrogen (details are shown in the ESI†), which inhibits the further aggregation and alignment of metal hydroxide nuclei, resulting in the formation of an amorphous structure.[10] Systematic optimization revealed that this specific Ni/Fe ratio and $NaBH_4$ concentration achieve the ideal balance between structural amorphization and catalytic performance, demonstrating optimal activity and stability among all tested compositions (Fig. S1 and S2, ESI†). And the borate-free amorphous nickel–iron hydroxides (a-NiFeO$_x$H$_y$) were synthesized using the similar method without the addition of $NaBH_4$ to the alkaline solution. For comparison, crystalline NiFe LDH was prepared *via* the conventional hydrothermal method.

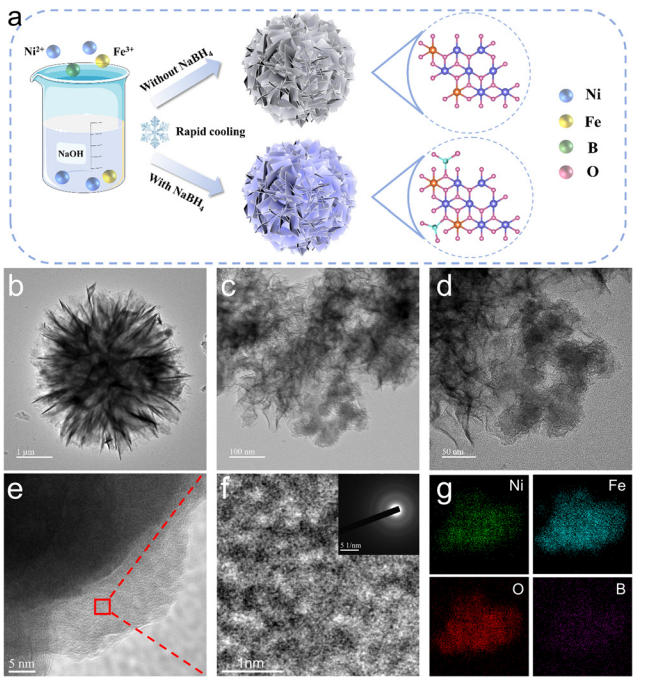

Fig. 1 Morphological characterization of a-B-NiFeO$_x$H$_y$. (a) Schematic diagram of the synthesis of a-B-NiFeO$_x$H$_y$ and a-NiFeO$_x$H$_y$. (b)–(d) TEM, (e) and (f) high-resolution TEM (selected area electron diffraction), and (g) elemental mapping images of a-B-NiFeO$_x$H$_y$.

The as-prepared catalysts display a nanosheet-assembled nanoflower structure (Fig. 1b–d and Fig. S3–S5, ESI†), revealed through scanning electron microscopy (SEM) and transmission electron microscopy (TEM). Notably, the amorphous structure characteristics of a-B-NiFeO$_x$H$_y$ (Fig. 1e and f) and a-NiFeO$_x$H$_y$ (Fig. S4, ESI†) are confirmed by high-resolution TEM (HRTEM), from which no discernible lattice fringes can be observed. Besides, neither obvious bright spots nor clear diffraction rings can be discerned in the selected area electron diffraction (SAED) patterns, manifesting the amorphousness of a-B-NiFeO$_x$H$_y$ and a-NiFeO$_x$H$_y$ (Fig. 1f).[11] In sharp contrast, the NiFe LDH counterpart exhibits clear lattice fringes and diffraction spots, suggesting the well-crystalline structure. Elemental mapping images (Fig. 1g) illustrate the uniform distribution of Ni, Fe, B, and O elements in a-B-NiFeO$_x$H$_y$, with the mass fraction of B being 2.98%, verifying the effective incorporation of B. The X-ray diffraction (XRD) patterns of a-NiFeO$_x$H$_y$ and a-B-NiFeO$_x$H$_y$ show similar diffraction peaks, which validate that the borate incorporation does not alter the lattice structure. (Fig. 2a). The broad diffraction peak reflects the lack of a long-range ordered structure, while the peak around 35° exhibiting broadened asymmetry indicates the presence of more defects and disordered regions in the sample. These XRD features are consistent with the characteristics of amorphous materials.[12] By contrast, the NiFe LDH shows typical diffraction peaks located at 11.4°, 22.9° and 33.5° corresponding to the (003), (006) and (012) planes of the layered double hydroxide crystalline structure.[13]

To further investigate the chemical structure of a-NiFeO$_x$H$_y$ and a-B-NiFeO$_x$H$_y$, Fourier transform infrared (FTIR) spectroscopy and Raman spectroscopy were employed. The FTIR (Fig. 2b) spectrum of a-B-NiFeO$_x$H$_y$ exhibits absorption peaks at 975 cm^{-1} and 1280 cm^{-1}, which are assigned as the vibrations of BO_3^{3-}.[14] Moreover, the Raman peak at 287 cm^{-1} corresponding to the B–O bonds is also discerned for a-B-NiFeO$_x$H$_y$ (Fig. S6, ESI†). These findings confirm the successful incorporation of BO_3^{3-} into the amorphous a-B-NiFeO$_x$H$_y$. The borate incorporation process is accompanied by release of hydrogen gas, which would enrich the pore structure *via* the foaming effect. Brunauer–Emmett–Teller (BET) analysis was performed to validate the hypothesis (Fig. S7, ESI†).[15] The a-B-NiFeO$_x$H$_y$ exhibits type-IV isotherms with a hysteresis loop at high relative pressure, suggesting the dominated mesoporous structure. Besides, the specific surface area of a-B-NiFeO$_x$H$_y$ (224.83 m^2 g^{-1}) is significantly larger than that of a-NiFeO$_x$H$_y$ (45.03 m^2 g^{-1}). The mesoporous structure and the large specific surface area are beneficial for exposing more active sites, facilitating mass transport, and thereby improving the OER performance.

The chemical composition and electronic structure were then examined by a series of characterization studies. The inductively coupled plasma optical emission spectrometry (ICP-OES) analysis reveals that the Ni/Fe ratio in all three catalysts is consistently close to 3 : 1, in agreement with the feeding ratio (Tables S1 and S2, ESI†). The successful incorporation of BO_3^{3-} in a-B-NiFeO$_x$H$_y$ is confirmed by X-ray photoelectron spectroscopy (XPS), which shows a characteristic peak of B–O at ~192 eV (Fig. 2c).[16] Ni 2p XPS (Fig. S8a, ESI†) of a-B-NiFeO$_x$H$_y$ exhibits two peaks at 855.52 eV and 873.14 eV, corresponding to Ni^{2+} $2p_{3/2}$ and Ni^{2+} $2p_{1/2}$,[17] respectively, which represents a positive shift of 0.12 eV compared with a-NiFeO$_x$H$_y$ (Fig. S9a, ESI†). While the Fe 2p XPS (Fig. S8b and S9b, ESI†) remains nearly unchanged upon doping BO_3^{3-}, where four peaks at 710.52 eV, 713.51 eV, 724.55 eV and 727.85 eV, attributable to Fe^{2+} $2p_{3/2}$, Fe^{3+} $2p_{3/2}$, Fe^{2+} $2p_{1/2}$ and Fe^{3+} $2p_{1/2}$,[18] respectively, are clearly identified. The XPS results show no detectable characteristic signals for metallic Ni or Fe, indicating that Ni and Fe predominantly exist in their oxidized states rather than as metallic particles. Notably, the O 1s spectra (Fig. S10, ESI†) reveal a lower proportion of oxygen vacancies in a-B-NiFeO$_x$H$_y$ (36.8%) compared to a-NiFeO$_x$H$_y$ (52.2%), in line with the weaker electron paramagnetic resonance (EPR) signals (Fig. 2d) observed for a-B-NiFeO$_x$H$_y$.[19] Positron annihilation spectroscopy quantitatively confirms this vacancy occupation mechanism (Fig. S11 and Tables S3, S4, ESI†), showing a 36.9% reduction in oxygen vacancy concentration (I_2 intensity decrease from 68.36% to 43.11%) accompanied by characteristic lifetime elongation (0.3189 ns to 0.3371 ns), which reflects the modified electronic environment of residual vacancies due to BO_3^{3-} incorporation. These findings demonstrate that BO_3^{3-} is introduced into a-B-NiFeO$_x$H$_y$ by occupying oxygen vacancies within the amorphous NiFe lattice.

The local structure of the materials was further investigated using X-ray absorption spectroscopy (XAS). The Ni K-edge X-ray absorption near-edge structure (XANES) spectra (Fig. 2e) show a positive shift of the absorption edge toward higher energy in a-B-NiFeO$_x$H$_y$ *versus* a-NiFeO$_x$H$_y$ counterpart, signifying a higher valence state of Ni through metal-to-ligand charge transfer.[20] In contrast, an insignificant change of the

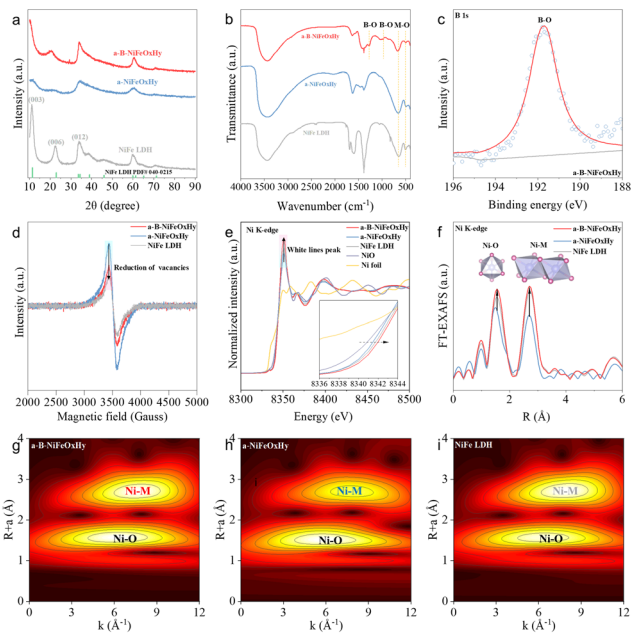

Fig. 2 Structural characterization of a-B-NiFeO$_x$H$_y$. (a) XRD patterns. (b) FTIR spectra. (c) B 1s XPS of a-B-NiFeO$_x$H$_y$. (d) EPR spectra. (e) Ni K-edge of XANES spectra. (f) Ni K-edge of Fourier-transform EXAFS spectra. (g)–(i) The WT contour plots of a-B-NiFeO$_x$H$_y$, a-NiFeO$_x$H$_y$ and NiFe LDH.

absorption edge is discerned in the Fe K-edge XANES spectra of a-B-NiFeO$_x$H$_y$ and a-NiFeO$_x$H$_y$ (Fig. S12, ESI†). We further performed a systematic correlation between the absorption edge position (E_0) and the known oxidation states of the reference compounds and constructed calibration curves for both Ni and Fe. Quantitative analysis reveals that the average oxidation states of Ni are +2.22 in a-B-NiFeO$_x$H$_y$ and +2.06 in a-NiFeO$_x$H$_y$, while Fe oxidation states are +2.58 and +2.52, respectively (Fig. S13, ESI†), indicating that the introduction of BO_3^{3-} increased the oxidation state of Ni while leaving the oxidation state of Fe unchanged. This observation is consistent with the XPS results. The doping effect on the coordination environment was then checked. To be specific, Ni K-edge k^3-weighted extended X-ray absorption fine structure (EXAFS) analysis reveals larger oscillation amplitudes of a-B-NiFeO$_x$H$_y$ than that of a-NiFeO$_x$H$_y$, suggesting an increase in the average coordination number (CN) of Ni after the incorporation of BO_3^{3-} (Fig. S14, ESI†).[21] The EXAFS spectra (Fig. 2f) disclose the presence of Ni–O and Ni–M coordination shells in both a-B-NiFeO$_x$H$_y$ and a-NiFeO$_x$H$_y$,[22] whereas a-B-NiFeO$_x$H$_y$ displays a higher intensity of the Ni–O peak, further confirming the increase in the coordination number of Ni after the filling of oxygen vacancies by BO_3^{3-}.[23] The noticeable elongation of Ni–O bonds in a-B-NiFeO$_x$H$_y$ further confirms that the introduction of borate anions inhibits the contraction of metal–oxygen bonds typically associated with the formation of oxygen vacancies, thereby enhancing the structural stability of the catalyst. Similarly, the signal intensity of the second coordination shell (Ni–M) in a-B-NiFeO$_x$H$_y$ is also significantly enhanced compared to that in a-NiFeO$_x$H$_y$, as further supported by wavelet transform (WT) analysis (Fig. 2g). In NiFe hydroxides, Ni and Fe atoms are bridged *via* lattice oxygen; thus, the enhanced Ni–M signal suggests that the filling of oxygen vacancies by BO_3^{3-} formed a more stable bridging structure with metal sites, leading to stronger intermetallic interactions.[24] A more robust Ni–O–M bridging oxygen structure is beneficial for facilitating electron transfer between Ni and Fe during the OER process, which can also suppress metal leaching or lattice degradation towards simultaneously improved activity and stability.[25]

The OER performance of the prepared catalysts was systematically evaluated in 1.0 M KOH electrolyte. The polarization curves (Fig. 3a) reveal that a-B-NiFeO$_x$H$_y$ exhibits significantly higher OER activity compared to a-NiFeO$_x$H$_y$ and NiFe LDH. In particular, a-B-NiFeO$_x$H$_y$ achieves current densities of 10 and 100 mA cm^{-2} at low overpotentials (η) of 234 and 288 mV (Fig. 3b), respectively. In contrast, a-NiFeO$_x$H$_y$ requires overpotentials of 280 and 337 mV to reach the same current densities, highlighting the superior catalytic performance of a-B-NiFeO$_x$H$_y$. The boosted OER kinetics of a-B-NiFeO$_x$H$_y$ is also certified by the lower Tafel slope of 30.1 mV dec^{-1} than those of a-NiFeO$_x$H$_y$ (41.1 mV dec^{-1}) and NiFe LDH (57.2 mV dec^{-1}) (Fig. 3c). To investigate the origins of the enhanced catalytic activity on a-B-NiFeO$_x$H$_y$, the double-layer capacitance (C_{dl}) was estimated (Fig. S15, ESI†) to evaluate its electrochemical active surface area (ECSA), as C_{dl} is typically proportional to the ECSA of an electrocatalyst. The results show that a-B-NiFeO$_x$H$_y$ has a significantly

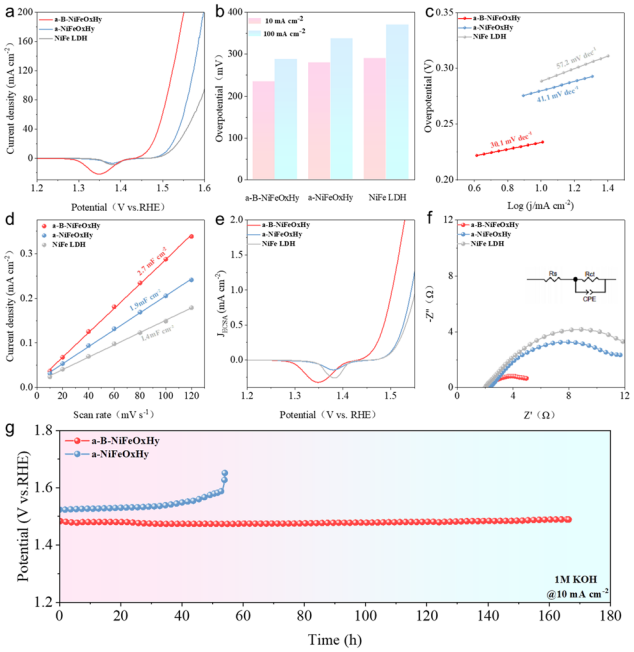

Fig. 3 Electrocatalytic performance of a-B-NiFeO$_x$H$_y$. (a) Polarization curves of various samples for the OER. (b) Overpotentials of a-B-NiFeO$_x$H$_y$, a-NiFeO$_x$H$_y$ and NiFe LDH to achieve the current densities of 10 and 100 mA cm^{-2}. (c) Tafel plots of a-B-NiFeO$_x$H$_y$, a-NiFeO$_x$H$_y$ and NiFe LDH. (d) Capacitance. (e) ECSA-normalized LSV curves. (f) Nyquist plots. (g) CP curves of a-B-NiFeO$_x$H$_y$ and a-NiFeO$_x$H$_y$.

higher C_{dl} (Fig. 3d) value (2.7 mF cm^{-2}) than a-NiFeO$_x$H$_y$ (1.9 mF cm^{-2}), indicating more accessible active sites of a-B-NiFeO$_x$H$_y$. Furthermore, the intrinsic activity of different catalysts was also compared by normalizing the OER current by ECSA (Fig. 3e). Obviously, across the whole potential window, a-B-NiFeO$_x$H$_y$ exhibits superior intrinsic activity, which may be attributed to the optimized electronic structure of Ni active sites following the incorporation of BO_3^{3-}. Moreover, Nyquist plots (Fig. 3f) reveal that the charge transfer resistance of a-B-NiFeOxHy is significantly lower than that of a-NiFeO$_x$H$_y$, indicating accelerated charge transfer kinetics on a-B-NiFeO$_x$H$_y$.

We further investigated the promotion effect of BO_3^{3-} anion incorporation on electrochemical stability through accelerated degradation tests. After 1000 cyclic voltammetry (CV) cycles (Fig. S17, ESI†), the a-B-NiFeO$_x$H$_y$ electrocatalyst exhibits negligible degradation in OER performance, while a positive shift of 20 mV in overpotential at 20 mA cm^{-2} is observed on a-NiFeO$_x$H$_y$, demonstrating enhanced stability upon BO_3^{3-} anion incorporation. The exceptional durability of the as-synthesized a-B-NiFeO$_x$H$_y$ for the OER is further corroborated by chronoamperometry (CA) and chronopotentiometry (CP) tests (Fig. 3g and Fig. S16, S18–S20, ESI†). The decay rates for a-B-NiFeO$_x$H$_y$ are 0.04 mA h^{-1} and 0.03 mV h^{-1} for CA and CP, respectively, significantly lower than those of a-NiFeO$_x$H$_y$ (0.23 mA h^{-1} and 1.20 mV h^{-1}). To simulate the potential application of a-B-NiFeO$_x$H$_y$ in practical electrolyzers, its performance for overall water splitting (OWS) was evaluated in a two-electrode configuration (a-B-NiFeO$_x$H$_y$‖Pt/C). Remarkably, a-B-NiFeO$_x$H$_y$‖Pt/C

only requires the cell voltages of 1.47, 1.65, and 1.82 V to deliver the current densities of 10, 50, and 100 mA cm^{-2}, respectively (Fig. S21, ESI†), lower than those of IrO_2‖Pt/C (1.50, 1.73 and 1.98 V). CP results of the a-B-$NiFeO_xH_y$‖Pt/C system demonstrate higher current densities at lower overpotentials for overall water splitting, along with no observable degradation after 30 hours of continuous operation, highlighting its long-term durability (Fig. S22, ESI†). These electrochemical measurements combined with characterization techniques collectively suggest that the introduction of BO_3^{3-} into the lattice oxygen vacancies endows a-B-$NiFeO_xH_y$ with a more robust M–O–M bridging oxygen structure and enhanced Ni–Fe interaction, thereby leading to a substantial improvement in its OER stability compared to a-$NiFeO_xH_y$ (Table S5, ESI†).

To comprehensively understand the influence of BO_3^{3-} on OER activity and stability, we monitored the dynamic structure evolution during the OER using XAS, XPS and Raman spectroscopy. The increase in white-line intensity and the positive shift in the absorption edge confirm the oxidation of Ni center during the OER process (Fig. S23, ESI†). Additionally, the enhanced Ni–M signal in the EXAFS spectra indicates a stronger coordination between Ni and Fe, as well as a tighter Ni–M metal bonding. These observations provide direct evidence for the transformation of NiFe hydroxide to NiFeOOH during the OER process.[26] Furthermore, the EXAFS curves (Fig. 4a and Fig. S24, ESI†) reveal a significant increase in the intensity of the Ni–O peak after the OER, indicating an increase in the coordination number (CN) of Ni in a-$NiFeO_xH_y$, consistent with the fitting results (increasing from 3.9 to 4.4, Fig. S25, ESI†). In contrast, the first coordination shell environment of Ni in a-B-$NiFeO_xH_y$ remains nearly unchanged (Fig. 4b and Fig. S26, ESI†) due to the stable Ni–O–M oxygen-bridged structure, demonstrating that the incorporation of BO_3^{3-} into lattice oxygen vacancies enhances the structural stability of the catalyst during the OER. The chemical state change after the OER was then examined by XPS. Compared to OER-treated a-$NiFeO_xH_y$ (Fig. S27–S29, ESI†), the Ni $2p_{3/2}$ peak of OER-treated a-B-$NiFeO_xH_y$ (Fig. 4c) exhibits a positive shift of 0.23 eV, while the Fe $2p_{3/2}$ peak (Fig. 4d) shows a negative shift of 0.49 eV, consistent with the higher Ni absorption edge energy (Fig. S30, ESI†) and lower Fe absorption edge energy (Fig. S31, ESI†) observed in the XANES spectra of OER-treated a-B-$NiFeO_xH_y$. These results unambiguously reveal the preferential oxidation of borate-bridged Ni sites in a-B-NiFeOxHy to high-valent Ni^{3+} during the OER process. This is further supported by the lower onset potential and peak position of the Ni^{2+} to Ni^{3+} transition in a-B-$NiFeO_xH_y$ (Fig. S32, ESI†).[27] Additionally, extensive studies have shown that under alkaline conditions and high anodic potentials, higher oxidation states of Fe are more susceptible to dissolution. The lower oxidation state of Fe in a-B-$NiFeO_xH_y$ is promising to suppress its dissolution.

Operando electrochemical Raman spectroscopy, which provides more insights into the dynamic evolution of Ni species during the OER (Fig. 4e, f and Fig. S33, ESI†), was performed. Two characteristic peaks at 475 cm^{-1} and 550 cm^{-1} can be found, corresponding to the E_g bending vibration mode and the A_{1g} stretching vibration mode of Ni^{3+}–O in NiOOH, respectively.[28] Compared to a-$NiFeO_xH_y$, the Ni^{3+}–O signal in a-B-$NiFeO_xH_y$ appears at a lower potential, indicating that the Ni species in a-B-$NiFeO_xH_y$ are more easily oxidized after the introduction of BO_3^{3-}. In the Raman spectrum, the A_{1g} peak corresponds to a more disordered vibrational mode, while the E_g peak represents a more ordered vibrational mode. Notably, the intensity ratio of the A_{1g} and E_g peaks (I_{550}/I_{475}) for a-B-$NiFeO_xH_y$ is much smaller than that of a-$NiFeO_xH_y$, indicating that the incorporation of BO_3^{3-} has filled some of the oxygen vacancies, thereby reducing the disordered vibrations and enhancing the ordered vibrations (Fig. S34 and S35, ESI†). This suggests that a-B-$NiFeO_xH_y$ possesses a more stable and ordered coordination structure.[29] Furthermore, the insignificant change in the I_{550}/I_{475} value with increasing voltage evidences BO_3^{3-} mediated structural stabilization that kinetically suppresses dynamic reconstruction, whereas a-$NiFeO_xH_y$ undergoes pronounced structure reconstruction.

The role of BO_3^{3-} incorporation into the host lattice in enhancing the OER electrocatalytic performance was further investigated using density functional theory (DFT) calculations. According to the experimental results, the models of a-NiFeOOH and BO_3^{3-}-doped a-NiFeOOH (denoted as a-B-NiFeOOH) were constructed (Fig. S36, ESI†). Charge density difference analysis (Fig. 5a and Fig. S37, ESI†) reveals that the introduction of BO_3^{3-} into the lattice oxygen vacancies significantly promotes electron transfer between the metal and oxygen. A strong electron depletion around the Ni atoms is observed, indicating partial electron transfer from Ni to O.[30] This observation is in line with the Bader charge analysis (Fig. S38, ESI†), which demonstrates decreased electron density of Ni in a-B-NiFeOOH configuration. The electron localization function (ELF) analysis quantitatively discloses the enhanced electron density localization at hydroxyl moieties coordinated to Ni centers in the BO_3^{3-}-incorporated sample, directly evidencing an increased oxidation state of Ni through ligand-induced charge polarization (Fig. 5b and Fig. S39, ESI†).

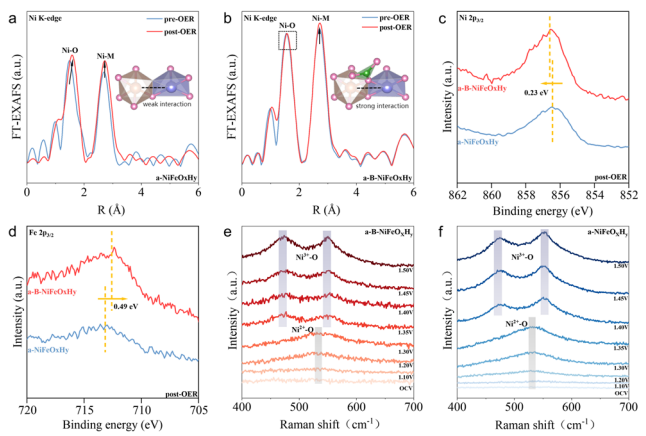

Fig. 4 Spectroscopic characterization of a-B-$NiFeO_xH_y$. (a) Ni K-edge of Fourier-transform EXAFS spectra in a-$NiFeO_xH_y$. (b) Ni K-edge of Fourier-transform EXAFS spectra in a-B-$NiFeO_xH_y$. (c) Ni $2p_{3/2}$ XPS spectrum of the catalyst after the OER. (d) Fe $2p_{3/2}$ XPS spectrum of the catalyst after the OER. (e) Electrochemical *in situ* Raman spectra of a-B-$NiFeO_xH_y$ in 1 M KOH solution. (f) Electrochemical *in situ* Raman spectra of a-$NiFeO_xH_y$ in 1 M KOH solution.

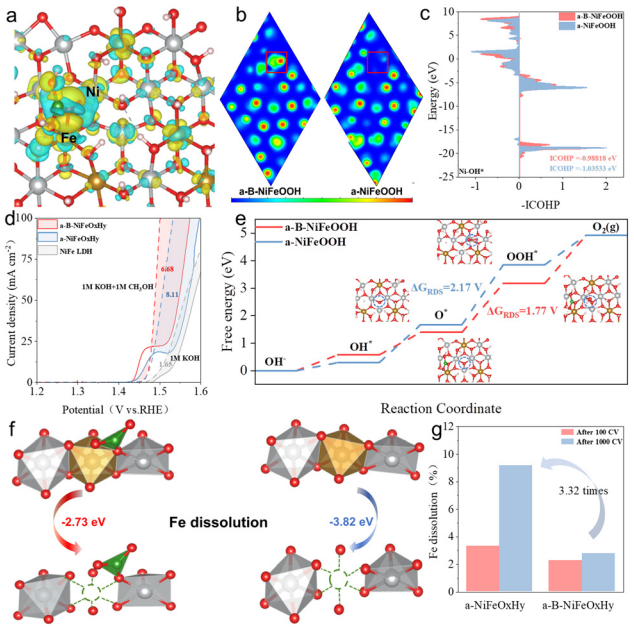

Fig. 5 DFT calculations. (a) Charge density difference diagrams (electron accumulation is in yellow and depletion in blue, respectively) of a-B-NiFeOOH. (b) ELF of a-B-NiFeOOH and a-NiFeOOH. The scale bar is located at the bottom, accompanied by a color scheme for viewing convenience. (Blue represents a fully delocalized electron state, while red represents a fully localized electron state.) (c) COHP analysis for a-B-NiFeOOH and a-NiFeOOH. (d) Polarization curves in 1 M KOH (without and with 1.0 mol L^{-1} methanol). (e) Gibbs free energy diagrams of OER intermediates over a-B-NiFeOOH and a-NiFeOOH. (f) The dissolution simulation of Fe in a-B-NiFeOOH and a-NiFeOOH. (g) Dissolution of Fe after CV cycling. The silver, yellow, red, white, and green atoms represent Ni, Fe, O, H, and B, respectively.

The regulated electronic states would affect the adsorption/desorption properties of OER intermediates. We then performed crystal orbital Hamilton population (COHP) analysis to analyze the bonding–antibonding property of Ni–O bonds, where a more positive integrated COHP (ICOHP) value indicates weaker bond strength. As shown in Fig. 5c, a-B-NiFeOOH exhibits a more positive ICOHP value compared to a-NiFeOOH, indicating weakened interaction between the metal active sites and oxygen intermediates after introducing BO_3^{3-}. Given the electrophilic nature of OH*, it can be probed through the reaction with nucleophilic alcohol molecules (*e.g.*, methanol and ethanol).[31] As shown in Fig. 5d, a-B-NiFeO$_x$H$_y$ exhibits a lower faradaic current from methanol oxidation compared to a-NiFeO$_x$H$_y$ (6.68 vs 8.11 mA cm^{-2} V), quantitatively demonstrating weaker OH* adsorption on the borate-modified surface. The decreased OH* adsorption is further corroborated by Laviron analysis (Fig. S40 and S41, ESI†),[32] which shows a smaller redox constant (K_s) of a-B-NiFeO$_x$H$_y$ than that of a-NiFeO$_x$H$_y$. *Operando* electrochemical impedance spectroscopy (EIS) coupled with Bode phase analysis (Fig. S42, ESI†) quantitatively resolves the accelerated dehydrogenation kinetics of OH*/OOH* intermediates on a-B-NiFeO$_x$H$_y$, evidenced by the obvious reduction in low-frequency region phase angle.[33] Based on the four-electron transfer mechanism, the Gibbs free energy (ΔG) for each elementary step of the OER, including the adsorption/desorption of different oxygen intermediates (OH*, O*, OOH*, and O_2), was calculated (Fig. 5e and Fig. S43, ESI†). The Gibbs free energy diagrams show that the weakened binding affinity with OH* on a-B-NiFeOOH lowers the thermodynamic barrier for the potential-determining OOH* formation step from 2.17 eV to 1.77 eV, thereby enhancing the OER catalytic activity.

To shed light on the enhanced stability, the dissolution behavior of Fe in both a-B-NiFeOOH and a-NiFeOOH during the OER process was examined as the previous studies revealed that Fe over-oxidation and dissolution under high anodic potentials are key factors affecting the stability of NiFe-based catalysts (Fig. 5f). The formation energy barrier of soluble Fe in a-B-NiFeOOH was calculated to be −2.73 eV, which is significantly higher than that in a-NiFeOOH (−3.82 eV). This indicates that the introduction of BO_3^{3-} into the lattice oxygen vacancies inhibits the dissolution of Fe, thus improving the catalyst's stability. The suppressed Fe dissolution is also certified by quantitative analysis of dissolved Fe ions after stability testing (Fig. 5g and Fig. S44 and S45, ESI†). In particular, the dissolution of Ni is significantly lower than that of Fe. During the first 100 cycles of CV activation, the Fe dissolution in both a-NiFeO$_x$H$_y$ and a-B-NiFeO$_x$H$_y$ is comparable. However, after the subsequent 1000 cycles of CV stability testing, only a small amount of Fe dissolved from a-B-NiFeO$_x$H$_y$, while Fe continued to dissolve

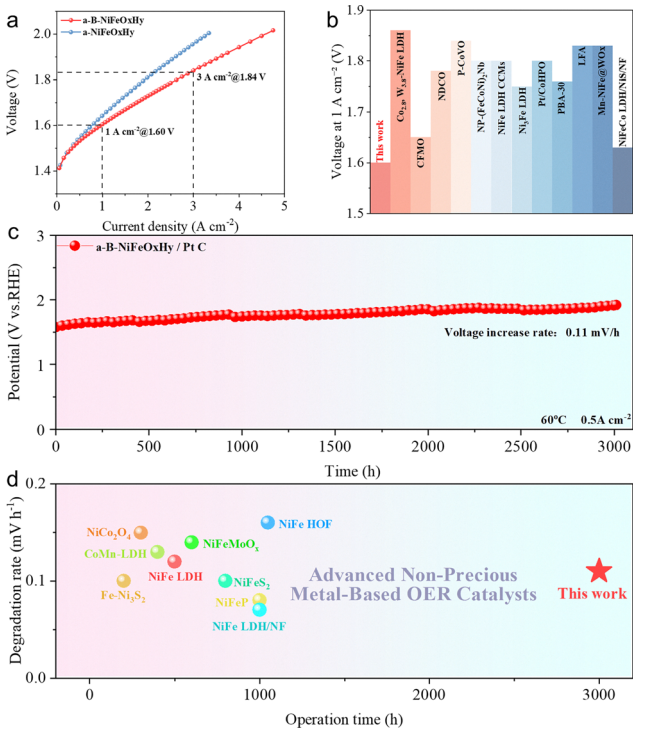

Fig. 6 AEMWE. (a) Polarization curves of the AEM electrolyzer obtained at 80 °C. (b) Comparison of the operational activity (voltage at 1 A cm^{-2}) of a-B-NiFeO$_x$H$_y$ with the reported anode catalysts. (c) CP curve of the AEM electrolyzer using the a-B-NiFeO$_x$H$_y$ catalyst operated at 0.5 A cm^{-2} at 60 °C. (d) Comparison of the operational stability (operation time and degradation rate) of a-B-NiFeO$_x$H$_y$ with the reported anode catalysts.

from a-NiFeO$_x$H$_y$. After the stability test, the Fe dissolution amounts from a-NiFeO$_x$H$_y$ are 3.32 times greater than that from a-B-NiFeO$_x$H$_y$, affording experimental evidence for the inhibited degradation of Fe on the more stable BO_3^{3-} incorporated a-NiFeOOH structure.

Considering the high activity and stability of a-B-NiFeO$_x$H$_y$ for the OER, we assembled an AEMWE device using a-B-NiFeO$_x$H$_y$ as the anode catalyst to evaluate its potential for practical application. The steady-state polarization curve of a-B-NiFeO$_x$H$_y$ shows significantly higher performance (Fig. 6a). In particular, industrial-level current densities (Fig. 6b) of 1, 2, and 3 A cm^{-2} were achieved at low cell voltages of only 1.60 V, 1.72 V, and 1.84 V, respectively, which are markedly superior to those of a-NiFeO$_x$H$_y$ (1.66 V at 1 A cm^{-2}, 1.83 V at 2 A cm^{-2}, and 1.95 V at 3 A cm^{-2}). Notably, the electrolyzer can reach a high current density of 4.75 A cm^{-2} at 2 V (Fig. S46, ESI†). Additionally, a-B-NiFeO$_x$H$_y$ also exhibits unprecedented long-term stability by continuously operating at 0.5 A cm^{-2} for 3000 h, with a voltage decay of only 0.11 mV h^{-1}, highlighting its significant potential for practical applications in the AEMWE (Fig. 6c and Fig. S47, ESI†). Overall, the a-B-NiFeO$_x$H$_y$ anode electrolyzer outperforms the majority of reported non-precious metal catalyst-based anode electrolyzers in terms of both activity and, particularly, stability (Fig. 6d).

Conclusions

In summary, this work presents an effective strategy for addressing the stability issue of amorphous NiFe-based OER electrocatalysts by incorporating BO_3^{3-} into the oxygen vacancy site. Mechanistic investigations reveal that the incorporated BO_3^{3-} not only optimizes the coordination environment of Ni atoms towards stabilizing the Ni–O–Fe oxygen-bridge framework but also facilitates electron transfer from Ni to Fe. This efficient electron transfer increases the dissolution energy barrier of Fe by 1.09 eV, thus suppressing its oxidation and dissolution for enhanced electrochemical stability. *Operando* spectroscopic analyses and theoretical calculations demonstrate that the electron redistribution promotes the formation of high-valence Ni^{3+} active species and optimizes oxygen intermediate adsorption towards faster OER kinetics. These attributes endow the a-B-NiFeO$_x$H$_y$ catalyst with unprecedented activity and stability when used as the anode in the AEMWE, delivering a high current density of 4.75 A cm^{-2} at 2.0 V cell voltage, while maintaining ultra-long-term stability over 3000 hours at 0.5 A cm^{-2}. This work provides fundamental insights into the rational design of high-performance amorphous electrocatalysts for sustainable water splitting applications.

Author contributions

W. Xing and J. Zhu supervised the project. J. Zhu proposed the concept. W. Qi performed the experiments and wrote the manuscript. M. Xiao and L. Wang revised the manuscript. K. Li conducted the DFT calculations. Y. Zeng helped with implementing the experiment. All authors participated in data analysis and manuscript discussion.

Conflicts of interest

There are no conflicts to declare.

Data availability

The data that support the findings of this study are available from the corresponding author upon reasonable request.

Acknowledgements

This work was financially supported by the National Natural Science Foundation of China (22279129) and the Jilin Province Science and Technology Development Program (20230101367JC and 20230201154GX). We thank the Shanghai Synchrotron Radiation Facility for conducting the X-ray absorption spectroscopy experiments at the BL17B1 station. The computational work was supported by the high-performance computing center of Jilin Province.

Notes and references

1 J. T. Li, *Nano-Micro Lett.*, 2022, **14**, 122.
2 M. Chen, N. Kitiphatpiboon, C. R. Feng, A. Abudula, Y. F. Ma and G. Q. Guan, *eScience*, 2023, **3**, 100111.
3 J. Q. Wang, Y. Liu, G. C. Yang, Y. Q. Jiao, Y. M. Dong, C. G. Tian, H. J. Yan and H. G. Fu, *Nat. Commun.*, 2025, **16**, 1319.
4 B. H. Yao, Y. T. Chen, Y. Y. Yan, Y. Yang, H. H. Xing, Y. C. Xu, D. X. Jiao, Z. C. Xing, D. W. Wang and X. R. Yang, *Angew. Chem., Int. Ed.*, 2024, **64**, e202416141.
5 J. Zhao, J. J. Zhang, Z. Y. Li and X. H. Bu, *Small*, 2020, **16**, 2003916.
6 L. Yang, Z. Liu, S. Zhu, L. Feng and W. Xing, *Mater. Today Phys.*, 2021, **16**, 100292.
7 W. Wang, Z. X. Wang, Y. C. Hu, Y. C. Liu and S. L. Chen, *eScience*, 2022, **2**, 438–444.
8 H. X. Liao, G. H. Ni, P. F. Tan, K. Liu, X. Z. Liu, H. L. Liu, K. J. Chen, X. S. Zheng, M. Liu and J. Pan, *Adv. Mater.*, 2023, **35**, 2300347.
9 Y. H. Hu, T. Y. Shen, Z. H. Wu, Z. H. Song, X. L. Sun, S. Y. Hu and Y. F. Song, *Adv. Funct. Mater.*, 2025, **35**, 2413533.
10 Y. Duan, Z. Y. Yu, S. J. Hu, X. S. Zheng, C. T. Zhang, H. H. Ding, B. C. Hu, Q. Q. Fu, Z. L. Yu, X. Zheng, J. F. Zhu, M. R. Gao and S. H. Yu, *Angew. Chem., Int. Ed.*, 2019, **58**, 15772–15777.
11 C. Y. Guo, Y. M. Shi, S. Y. Lu, Y. F. Yu and B. Zhang, *Chin. J. Catal.*, 2021, **42**, 1287–1296.
12 Z. Li, Y. E. Zhou, M. H. Xie, H. Cheng, T. Wang, J. Chen, Y. Lu, Z. L. Tian, Y. Q. Lai and G. H. Yu, *Angew. Chem., Int. Ed.*, 2023, **62**, e202217815.

13 J. Y. Wang, Z. Y. Xing, R. Y. Kang, Y. J. Zheng, Z. Zhang, T. Ma, Y. Wang, B. Yin, Y. Z. Liao, L. Li, C. Cheng and S. Li, *Adv. Funct. Mater.*, 2024, **35**, 2418439.
14 H. X. Liao, G. H. Ni, P. F. Tan, Y. Liu, K. J. Chen, G. M. Wang, M. Liu and J. Pan, *Appl. Catal., B*, 2022, **317**, 121713.
15 S. Q. Wang, W. Y. Huo, H. C. Feng, Z. H. Xie, J. K. Shang, E. V. Formo, P. H. C. Camargo, F. Fang and J. Q. Jiang, *Adv. Mater.*, 2023, **35**, 2304494.
16 Y. K. Bai, Y. Wu, X. C. Zhou, Y. F. Ye, K. Q. Nie, J. O. Wang, M. Xie, Z. X. Zhang, Z. J. Liu, T. Cheng and C. B. Gao, *Nat. Commun.*, 2022, **13**, 6094.
17 X. Li, Z. Xie, S. Roy, L. Gao, J. Liu, B. Zhao, R. Wei, B. Tang, H. Wang, P. Ajayan and K. Tang, *Adv. Mater.*, 2024, **37**, e2410295.
18 R. Li, R. Y. Wu, Z. B. Li, J. Wang, X. J. Liu, Y. R. Wen, F. K. Chiang, S. W. Chen, K. C. Chan and Z. P. Lu, *Adv. Mater.*, 2023, **35**, 2206890.
19 Y. Wang, P. Guo, J. Zhou, B. Bai, Y. F. Li, M. R. Li, P. Das, X. H. Wu, L. J. Zhang, Y. Cui, J. P. Xiao and Z. S. Wu, *Energy Environ. Sci.*, 2024, **17**, 8820–8828.
20 X. Z. Su, Y. Wang, J. Zhou, S. Q. Gu, J. Li and S. Zhang, *J. Am. Chem. Soc.*, 2018, **140**, 11286–11292.
21 J. T. Ding, D. Y. Guo, N. S. Wang, H. F. Wang, X. F. Yang, K. Shen, L. Y. Chen and Y. W. Li, *Angew. Chem., Int. Ed.*, 2023, **62**, e202311909.
22 Y. D. Yao, G. M. Zhao, X. Y. Guo, P. Xiong, Z. H. Xu, L. H. Zhang, C. S. Chen, C. Xu, T. S. Wu, Y. L. Soo, Z. M. Cui, M. M. J. Li and Y. Zhu, *J. Am. Chem. Soc.*, 2024, **146**, 15219–15229.
23 S. L. Zhao, C. H. Tan, C. T. He, P. F. An, F. Xie, S. Jiang, Y. F. Zhu, K. H. Wu, B. W. Zhang, H. J. Li, J. Zhang, Y. Chen, S. Q. Liu, J. C. Dong and Z. Y. Tang, *Nat. Energy*, 2020, **5**, 881–890.
24 H. X. Liao, K. J. Chen, X. R. He, J. X. Tong, X. Z. Liu, P. F. Tan, X. Y. Guo and J. Pan, *Nano Lett.*, 2024, **24**, 15436–15443.
25 H. Wu, J. W. Chang, J. K. Yu, S. Y. Wang, Z. Hu, G. I. N. Waterhouse, X. Yong, Z. Y. Tang, J. B. Chang and S. Y. Lu, *Nat. Commun.*, 2024, **15**, 10315.
26 X. Luo, H. Zhao, X. Tan, S. Lin, K. Yu, X. Mu, Z. Tao, P. Ji and S. Mu, *Nat. Commun.*, 2024, **15**, 8293.
27 L. S. Peng, N. Yang, Y. Q. Yang, Q. Wang, X. Y. Xie, D. Sun-Waterhouse, L. Shang, T. R. Zhang and G. I. N. Waterhouse, *Angew. Chem., Int. Ed.*, 2021, **60**, 24612–24619.
28 M. Han, C. H. Wang, J. Zhong, J. R. Han, N. Wang, A. Seifitokaldani, Y. F. Yu, Y. C. Liu, X. H. Sun, A. Vomiero and H. Y. Liang, *Appl. Catal., B*, 2022, **301**, 120764.
29 Y. J. Wu, J. Yang, T. X. Tu, W. Q. Li, P. F. Zhang, Y. Zhou, J. F. Li, J. T. Li and S. G. Sun, *Angew. Chem., Int. Ed.*, 2021, **60**, 26829–26836.
30 Q. Y. Wang, Y. J. Gong, X. Zi, L. Gan, E. Pensa, Y. X. Liu, Y. S. Xiao, H. M. Li, K. Liu, J. W. Fu, J. Liu, A. Stefancu, C. Cai, S. Y. Chen, S. G. Zhang, Y. R. Lu, T. S. Chan, C. Ma, X. Y. Cao, E. Cortes and M. Liu, *Angew. Chem., Int. Ed.*, 2024, **63**, e202405438.
31 H. B. Tao, Y. H. Xu, X. Huang, J. Z. Chen, L. J. Pei, J. M. Zhang, J. G. G. Chen and B. Liu, *Joule*, 2019, **3**, 1498–1509.
32 Y. Huang, L. W. Jiang, B. Y. Shi, K. M. Ryan and J. J. Wang, *Adv. Sci.*, 2021, **8**, 2101775.
33 Y. Du, F. K. Xie, M. F. Lu, R. X. Lv, W. X. Liu, Y. D. Yan, S. C. Yan and Z. G. Zou, *Nat. Commun.*, 2024, **15**, 1780.